In-situ synthesis of single-atom Ir by utilizing metal-organic frameworks: An acid-resistant catalyst for hydrogenation of levulinic acid to c-valerolactone

Wenxiu Cao [a,b,1], Lu Lin [a,1], Haifeng Qi [a,c], Qian He [d], Zhijie Wu [e], Aiqin Wang [a,⇑], Wenhao Luo [a,⇑], Tao Zhang [a]

[a] State Key Laboratory of Catalysis, Dalian Institute of Chemical Physics, Chinese Academy of Sciences, Dalian 116023, China
[b] College of Chemistry and Chemical Engineering, Jishou University, Jishou 416000, China
[c] University of Chinese Academy of Sciences, Beijing 100049, China
[d] Cardiff Catalysis Institute, School of Chemistry, Cardiff University, Cardiff CF10 3AT, United Kingdom
[e] State Key Laboratory of Heavy Oil Processing and the Key Laboratory of Catalysis of CNPC, China University of Petroleum, Beijing 102249, China

a r t i c l e i n f o

Dedication to 70th anniversary of Dalian Institute of Chemical Physics, Chinese Academy of Sciences.

Keywords:
Biomass
Catalyst stability
Levulinic acid
In-situ synthesis
Single-atom catalysis

a b s t r a c t

The hydrogenation of levulinic acid (LA) to c-valerolactone (GVL) is a key reaction for the production of renewable chemicals and fuels, wherein acid-resistant and robust catalysts are highly desired for practi-cal usage. Herein, an ultra-stable 0.6 wt% Ir@ZrO_2@C single-atom catalyst was prepared via an in-situ synthesis approach during the assembly of UiO-66, followed by confined pyrolysis. The Ir@ZrO_2@C offered not only a quantitative LA conversion and an excellent GVL selectivity (>99%), but also an unprecedented stability during recycling runs under harsh conditions (at T = 453 K, P_{H2} = 40 bar in pH = 3 or pH = 1 aqueous solution). By thorough spectroscopy characterizations, a well-defined structure of atomically dispersed Ir^{d+} atoms onto nano-tetragonal ZrO_2 confined in the amorphous carbon was identified for the Ir@ZrO_2@C. The strong metal-support interaction and the confinement of the amor-phous carbon account for the ultra-stability of the Ir@ZrO_2@C.

1. Introduction

The increasing energy appetite of an ever-growing global popu-lation, the accumulation of CO_2 in the atmosphere, price fluctua-tions and dwindling supplies of the fossil fuel, as well as legislation and mandates, have all stimulated the search for alter-native feedstock for chemicals and fuels productions [1,2]. Biomass is one particularly promising, alternative and abundant feedstock, which has been explored for fuels and chemicals production [3,4]. A small group of valuable chemical intermediates have emerged and served as platform molecules, which have the poten-tial to play a key role as primary biorefinery building blocks [5]. Levulinic acid (LA) is identified as one of the most promising biomass-derived platform molecules [6,7], and many value-added chemicals can be produced from LA, including renewable solvents, plasticizers, polymer monomers, pharmaceutical formulations, and fuel components and additives [8,9]. c-valerolactone (GVL), a ver-satile platform molecule in its own right, is actually involved as an intermediate in many of those upgrading routes, making the hydrogenation of LA to GVL a reaction of great importance in bio-mass valorization [10,11].

Processes for upgrading biomass-derived platform molecules are mainly operated in liquid phase at a high temperature and pressure, and the reaction medium is normally highly oxygen-functionalized, polar and even corrosive [12,13]. Such harsh condi-tions can raise significant challenges for the catalyst stability. Most metal catalysts such as ruthenium [14,15], palladium [16], plat-inum [17], iridium [18,19] and etc., have shown promising perfor-mance in activity and selectivity for LA hydrogenation. However, they still suffer from catalyst deactivation and hardly survive in the polar and protic reaction medium, because the loss of active metal species arises from metal leaching and sintering during catalysis, resulting in significant loss of activity [20,21]. For exam-ple, the commercial Ru/C, well known for its high activity and

selectivity for LA hydrogenation, shows a poor reusability and durability in both batch [22] and continuous systems [23,24], and severe deactivation in a more acidic medium and long-term reactions was also reported [25]. This vulnerability in catalyst sta-bility has become a vast barrier for the development of durable cat-alysts in biomass valorization. Therefore, it is highly desired to develop acid-resistant and robust metal catalysts for liquid phase reactions in biomass conversions.

Fabricating single-atom catalysts (SACs) can form a strong chemical bond/interaction between the metal atoms and the underlying support, which affects the stability of single metal atoms [26,27]. Such interactions for improving catalyst stability were recently reported in biomass valorization. A NiANAC SAC with metal bonding strongly with the neighboring N atoms has delivered excellent stability for the direct conversion of cellulose into ethylene in aqueous phase at 518 K and 60 bar H_2, and no metal aggregation or leaching was observed after 7 consecutive runs [28]. Another $CoAMoS_2$ SAC with a strong covalent bond of isolated Co atoms to sulfur vacancies of MoS_2 monolayer sheets, showed enhanced catalyst stability compared to traditional $CoMoS_2$ for the hydrodeoxygenation of 4-methylphenol to toluene at 453 K and 30 bar H_2, without sulfur loss and deactivation after 7 cycles [29]. These first few examples show that the SACs approach can bring significant and positive impact on improving catalyst sta-bility, however, the application of SACs for the biomass-related condensed phase reactions in the polar and protic medium, is still limitedly reported and the efficient synthesis remains a grand challenge.

Ir-based catalysts have shown good hydrogenation ability in various hydrogen-involved reactions [30]. In the same manner, Ir-based homogeneous catalysts have already been reported with decent catalytic performance for the conversion of LA to GVL. For example, Wang and co-workers reported an iridium dipyridy-lamine catalyst to efficiently synthesis GVL by transfer hydrogena-tion of LA [19]. Another Ir pincer complex was also developed as an extremely active catalyst for this reaction, affording GVL in an excellent yield of 99% with a high TON of 71,000 [18]. However, difficulties in separation and recycling have hindered the further application of homogeneous catalysts. Heterogeneous Ir-based cat-alysts have been reported to be active for the hydrogenation of LA to GVL, such as carbon nanotube supported Ir nanoparticles [31] and Ir/C [14]. However, the GVL selectivity issue was shown for supported Ir nanoparticles owing to simultaneous generation of other byproducts by over hydrogenation [14], and the instability of the carbon-related material was also established due to the weak interaction between metal and supports. In this respect, we have devoted to developing a selective and stable Ir heterogeneous catalysts for the hydrogenation of LA to GVL via a SAC approach, which can readily bridge the advantages of typical homogeneous (nearly 100% metal atom utilization) and heterogeneous catalysts (ease in separation and recycling) [26].

Herein, we reported the first synthesis of an ultra-stable 0.6 wt% Ir@ZrO_2@C SAC via a facile method, which includes in-situ grafting of metal during assembly of UiO-66, followed by confined pyroly-sis. The catalytic performance of the Ir@ZrO_2@C SAC was compared to self-prepared, benchmark 2.7 wt% Ir/C and 0.6 wt% Ir/ZrO_2 nanocatalysts in the selective hydrogenation of LA to GVL. Notably, both of the catalysts showed significant deactivation during multi-ple reuse experiments in the polar and protic reaction media (pH = 3 and pH = 1) under harsh conditions (T = 453 K, P_{H2} = 40 bar), mainly owing to the leaching of Ir into the acidic reaction media. The Ir@ZrO_2@C SAC catalyst, showed an advantage in GVL selectivity and unprecedented stability, with no deactivation and metal sintering or leaching through 7 consecutive runs (pH = 3) and 6 consecutive runs (pH = 1) in an aqueous solution. Further insights into the structure and ultra-stability of Ir@ZrO_2@C were revealed by an extensive characterizations study with combination of various advanced techniques. The in-situ synthesis approach, via spatial confinement of single atoms into metal-organic framework, is shown to be an efficient method to prepare an acid-resistant solid catalyst.

2. Experimental

2.1. Preparation of materials

0.6 wt% Ir@ZrO_2@C SAC: In a typical synthesis, $ZrCl_4$ (1.2 mmol, 280 mg, 98%, Aladdin), H_2BDC (1.4 mmol, 235 mg, 99%, J&K), 4 mL CH_3COOH (99.5%, Tianjin Damao Chemical Reagent Factory), H_2IrCl_6 $6H_2O$ (4.2 10^{-3} mmol, 2.2 mg, 99%, Beijing Chemical Works) and 40 mL of N,N-dimethylformamide (DMF, 99%, Tianjin Kemiou Chemical Reagent Co., Ltd.) were treated under ultrasonication in a 100 mL Teflon-lined stainless steel auto-clave for 10 min. Then the mixture was heated up to 393 K and kept for 24 h. The obtained material was filtered and purified with DMF and ethanol (99%, Tianjin Kemiou Chemical Reagent Co., Ltd.), and then dried at 333 K overnight. The dried Ir@UiO-66 was heated to 873 K with a ramp of 5 K/min and pyrolyzed for 5 h in a nitrogen flow. A black powder was thus obtained when being cooled to room temperature, followed by reduction with $NaBH_4$ (98%, Tianjin Damao Chemical Reagent Factory) in methanol (99%, Tianjin Kemiou Chemical Reagent Co., Ltd.) at 353 K under reflux for 0.5 h. The resultant material was further filtered and washed first by H_2O and then ethanol, finally dried at 333 K overnight and denoted as Ir@ZrO_2@C. The Ir loading and carbon content in the Ir@ZrO_2@C material were 0.6 wt% and 28.8 wt% separately, as determined by ICP-OES (Table 1) and TG-DSC (Fig. S1).

2.7 wt% Ir/C nanocatalyst: An Ir/C nanocatalyst was prepared as the benchmark catalyst by the wet impregnation method previ-ously reported [32]. Activated carbon (540 mg, NORIT Nederland), 24 mL of H_2O and 18 mL of ethanol were treated under ultrasoni-cation for 30 min to form a homogeneous solution. H_2IrCl_6 $6H_2O$ (2.8 10^{-2} mmol, 15 mg) was then injected into the solution and stirred for 4 h. Next, 5 mol/L NaOH (99%, Tianjin Kemiou Chemical Reagent Co., Ltd.) aqueous solution was dropwise added to the above mentioned solution until the pH value was between 8 and 9. After introducing $NaBH_4$, the mixture was kept stirring for another 6 h. The resultant material was then filtered and washed first by H_2O and then ethanol, finally dried at 333 K overnight and denoted as Ir/C. The Ir content of the Ir/C material was about 2.7 wt%, as detected by ICP-OES (Table 1).

0.6 wt% Ir/ZrO_2 nanocatalyst: First of all, tetragonal ZrO_2 (t-ZrO_2) was prepared by following the method as previously reported [33,34]. $ZrO(NO_3)_2$ $6H_2O$ (12 mmol, 4.068 g, 99%, Alad-din), urea (34 mmol, 1.440 g, 99%, Tianjin Kemiou Chemical Reagent Co., Ltd.) and 30 mL of methanol were treated under ultra-sonication in a 100 mL Teflon-lined stainless steel autoclave for 10 min. Then the mixture was heated up to 448 K and kept for 20 h. The obtained material was filtered and purified with metha-nol and ethanol, and then dried at 333 K overnight. The dried solid was finally heated to 673 K with a ramp of 10 K/min and pyrolyzed for 4 h under static air to obtain t-ZrO_2. Ir nanoparticles supported on t-ZrO_2 was prepared by wet impregnation method. The as-prepared t-ZrO_2 powder as the support was first mixed with a requisite amount of H_2IrCl_6 $6H_2O$ solution at room temperature, followed by ultrasonication for 30 min. Then the slurry was stirred vigorously and the temperature was heated to 353 K until all the water had evaporated. After that, the sample was further dried at 333 K overnight. At last, the resultant material was reduced at 623 K for 2 h under 10% H_2/Ar flow and denoted as Ir/ZrO_2. The Ir loading is 0.6 wt%, as determined by ICP-OES (Table 1).

Table 1
Physicochemical properties of different samples under study.

Entry	Catalysts	S_{BET} (m^2/g)	Micropore surface area[a] (m^2/g)	External surface area[a] (m^2/g)	Micropore volume[a] (m^3/g)	Ir loading (wt%)	Ir loss (wt%)
1	UiO-66	1335	1275	80	0.484		
2	Ir@UiO-66	986	851	135	0.456		
3	ZrO_2@C	173	111	62	0.044		
4	Ir@ZrO_2@C fresh	155	77	78	0.042	0.6	
5	Ir@ZrO_2@C spent[b]	59	24	35	0.010	0.6	–[g, h]
6	Ir@ZrO_2@C spent[c]	17	3	14	0.002	0.6	–[g, i]
4	Ir/ZrO_2 fresh	108	–[f]	120	–[f]	0.61	
5	Ir/ZrO_2 spent[d]	99	–[f]	115	–[f]	0.57	6.7[h]
6	Ir/ZrO_2 spent[e]	73	5	68	0.002	0.53	12.5[i]
7	Ir/C fresh	538	296	242	0.157	2.7	
8	Ir/C spent[d]	589	345	244	0.178	2.5	5.8[h]
9	Ir/C spent[e]	533	327	205	0.168	2.6	3.7[i]

[a] Obtained by the t-plot method.
[b] After seven runs in a pH = 3 aqueous solution.
[c] After six runs in a pH = 1 aqueous solution.
[d] After three runs in a pH = 3 aqueous solution.
[e] After three runs in a pH = 1 aqueous solution.
[f] Below the limit of N_2 physisorption isotherms detection.
[g] Below the limit of ICP-OES detection.
[h] Detected by ICP-OES analysis of the reaction solution after the first run in a pH = 3 aqueous solution.
[i] Detected by ICP-OES analysis of the reaction solution after the first run in a pH = 1 aqueous solution.

2.2. Characterizations

Powder X-ray diffraction (XRD) measurements were performed on a PW3040/60 X' Pert PRO (PANalytical) diffractometer with a Cu Ka source (k = 0.15432 nm) at 40 kV and 40 mA. N_2 physisorption isotherms were performed on a Micromeritics ASAP 2460 instru-ment at 77 K, after outgassing of the samples at 523 K (ZrO_2@C, Ir@ZrO_2@C, Ir/C and Ir/ZrO_2) or 423 K (UiO-66, Ir@UiO-66) under vacuum for 12 h. Surface areas, micropore volumes and pore size distributions were determined by Brunauer-Emmett-Teller (BET) method, t-plot analysis and Barrett-Joyner-Halenda (BJH) method, respectively. Scanning transmission electron microscopy (STEM) images were obtained with a JEOL JEM-2100F microscope operated at 200 kV. Energy dispersive X-ray spectra (EDX-mapping) were collected with a JEOL Oxford X-MaxN 80 T silicon drift detector, by rastering the beam over the target zone. Aberration-corrected scanning transmission electron microscopy (AC-STEM) in the high angle annular dark field mode (AC-HAADF-STEM) were acquired by using an JEOL JEM ARM-200F STEM operating at 200 kV, located in the electron Physical Sciences Imaging Centre (ePSIC) at the Dia-mond Light Source. Inductively coupled plasma optical emission spectroscopy (ICP-OES) was introduced to determine the actual Ir loading of iridium catalysts using a Thermo Electron IRIS intrepid

II XSP instrument. X-Ray photoelectron spectroscopy (XPS) exper-iments were conducted on a Thermo Fisher ESCALAB 250Xi, and spectra were collected using an aluminum anode (Al Ka = 1486.6 eV). Temperature-programmed reduction of hydrogen (H_2-TPR) experiments were performed on a Micromeritics Auto Chem II 2920 equipped with a TCD detector. Before the H_2-TPR measurement, 90–100 mg of the sample was loaded into a U-shape quartz reactor and then treated at 473 K under Ar flow (30 mL min ^{1}) for 2 h to remove adsorbed species. After cooling to 300 K, the flowing gas was changed to a 10% H_2/Ar flow, and the sample was heated to 1000 K at a ramping rate of 5 K/min. All the obtained XPS spectra were regulated by the graphitic car-bon C 1s band (284.6 eV), for correcting the energy shift caused by electrostatic charging. Infrared spectroscopy (IR) using CO as the probe molecule was recorded on a BRUKER Equinox 55 spec-trometer (MCT detector). Each spectrum contained 32 scans and was collected with a resolution of 4 cm ^{1}. Self-supported catalyst wafers were tableted at 3 kbar pressure for 5 s and then put inside a self-designed cell with a CaF_2 window. The cell was first vacu-umed to 10^{-6} mbar and the wafer was then degassed at 573 K for 1 h with a heating ramp of 5 K/min. After cooling down to 85 K with liquid nitrogen, the cell was exposed to CO by a gas chamber, which could precisely control the CO injection amount by monitor-ing the gas pressure in the cell. IR-CO of the Ir@ZrO_2, obtained by burning off the amorphous carbon of the Ir@ZrO_2@C at 873 K for 5 h in the air, was studied at 87 K by stepwise increasing CO pressure.

2.3. Catalytic tests

The hydrogenation of LA to GVL was processed in batch auto-clave reactor at T = 453 K and P_{H2} = 40 bar. In a typical reaction, dif-ferent catalyst samples were mixed with 10 wt% LA aqueous solutions (the molar ratio of LA to Ir was kept at 500) in a 100 mL Parr autoclave reactor (Model 4792, Parr Instruments). For catalytic studies under more protic conditions, 0.2 mol/L HCI aqueous solution was added to tune the pH of the system to 1. Since the existence of hydrochloric acid could accelerate the dehy-dration process during LA-to-GVL transformation, LA to catalyst Ir molar ratio is fixed at 1000 in the case of 2.7 wt% Ir/C nanocatalyst to get a proper conversion level at a reaction time of 10 min under pH = 1. The reactor was closed and flushed three times with 10 bar N_2, then charged with 40 bar H_2, and heated to 453 K. The stirring speed in each run was set at 1200 rpm to avoid external mass transfer limitation and guarantee the reactions to be con-ducted in the kinetic regime [35]. After reaction, the reactor was cooled down to room temperature and H_2 was released. The liquid sample was separated by filtration for analysis and the solid cata-lyst was washed with water and acetone, and then dried overnight at 333 K. For recycling experiments, the obtained spent catalyst was collected for the next catalytic run with fresh substrate. All the components in the reaction mixture were analyzed by using an Agilent GC 7890 gas chromatograph equipped with an HP-INNOWax (30 m 0.32 mm) column and a flame ionization detector (FID). For the reactions at a pH value of 1, products were analyzed by an Agilent 1200 series high-performance liquid chro-matography (HPLC) with an HPX-87 column (ø8 300 mm) and a UV–vis detector. 5 mmol/L H_2SO_4 aqueous solutions as the

mobile phase, together with a flow rate of 0.5 mL/min was applied for HPLC at a column temperature of 328 K.

3. Results and discussion

3.1. Physicochemical characterizations of catalysts

The designed strategy to obtain 0.6 wt% Ir@ZrO_2@C SAC is illus-trated in Scheme 1. Firstly, a solution of H_2IrCl_6 as the Ir precursor is added into the synthetic solution of UiO-66. Notably, glacial acetic acid is added as modulator to produce missing-linker defects in UiO-66, which could expose AOH groups for anchoring Ir precursors [36,37]. As a result, Ir atoms are grafted into UiO-66 during its assembly process, in which atomic distribution of Ir species is achieved by dispersing mononuclear Ir precursors into metal-organic framework. The obtained Ir@UiO-66 material is subsequently pyrolyzed and followed by reduction to form an amorphous carbon confined composite. The obtained Ir@ZrO_2@C material possesses an enhanced hydrothermal stability than the parent UiO-66. Compared to the traditional post-modification strategy, such as impregnation methods, this in-situ synthesis strategy combines the processes of metal introduction and support formation into one pot synthesis, which is more promising for the techno-economic viability of material synthesis.

Fig. 1a displays the XRD patterns of Ir@UiO-66, UiO-66, Ir@ZrO_2@C and ZrO_2@C materials. The diffraction patterns of Ir@UiO-66 matches well with those of UiO-66, indicating that the addition of Ir precursors has limit influence on the assembly of the crystal structure of UiO-66. After thermally treated at 873 K for 5 h under N_2 atmosphere, the XRD pattern of Ir@ZrO_2@C shows similar reflection positions as UiO-66 pyrolysed ZrO_2@C, with fea-tured peaks of tetragonal ZrO_2 positioned at 2h = 30L, 35L, 50L and 60L, separately referring to the (1 1 1), (2 0 0), (2 2 0) and (3 1 1) lattice planes. The particle size of tetragonal ZrO_2 in Ir@ZrO_2@C cal-culated using the Scherer equation is about 3.0 nm in average. According to TG-DSC analysis (Fig. S1), the content of carbon spe-cies remained in Ir@ZrO_2@C is about 28.8 wt%. While the diffrac-tion peaks of crystallized carbon is absence in the XRD patterns, referring to the formation of amorphous carbon [38]. Additionally, no obvious iridium reflections are detected with this low Ir loading in the XRD pattern, indicating a well-dispersed Ir in the material. The porosities of different samples were analyzed by N_2-physisorption (Fig. 1b, Fig. S2 and Table 1). Ir@UiO-66 material affords two kinds of pore size centered at 0.54 and 0.68 nm, which are slightly lower than UiO-66 (0.64 and 0.87 nm). This might stem from the dispersion of Ir species into the micropores of UiO-66, as also corroborated by the decreased micropore volume and microp-ore surface area. After thermal pyrolysis, significant drop in poros-ity and the BET surface area is observed with both ZrO_2@C and Ir@ZrO_2@C, owing to destruction of porosity structure by burning organic linkers of UiO-66 into amorphous carbon during pyrolysis. Compared to ZrO_2@C, Ir@ZrO_2@C shows small drop in the micro-porosity and pore size distribution, pointing to the successful graft-ing of Ir in the Ir@ZrO_2@C. In addition, two benchmark catalysts, 2.7 wt% Ir/C nanocatalyst and 0.6 wt% Ir/ZrO_2, are also prepared. The Ir/C affords a typical micropore isotherm (Fig. S2) and a BET surface area of 538 m^2/g in N2 physisorption (Table 1). The corre-sponding pore size distribution shows pore sizes centered at 0.54

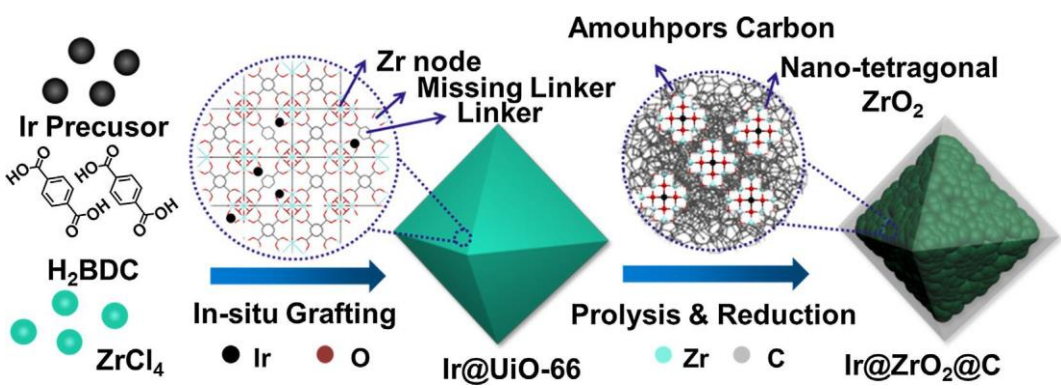

Scheme 1. Schematic illustration of the in-situ synthesis approach for the synthesis of 0.6 wt% Ir@ZrO_2@C.

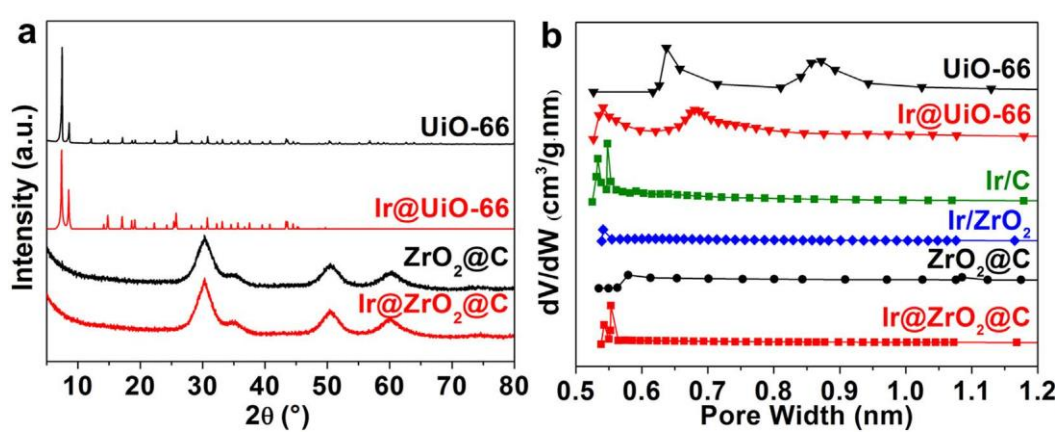

Fig. 1. (a) XRD patterns of UiO-66, Ir@UiO-66, ZrO_2@C, and Ir@ZrO_2@C; (b) pore size distribution of UiO-66, Ir@UiO-66, Ir/C, Ir//ZrO_2, ZrO_2@C and Ir@ZrO_2@C.

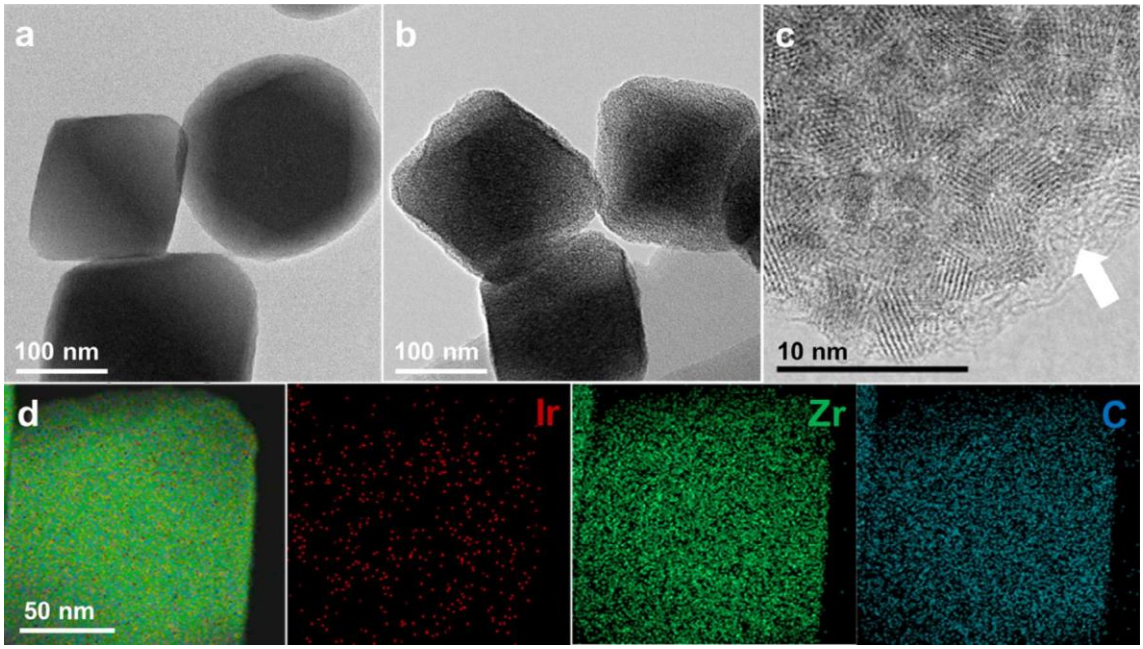

Fig. 2. STEM images of (a) Ir@UiO-66 and (b) 0.6 wt% Ir@ZrO_2@C; (c) high resolution STEM images, and (d) EDX-mapping analysis of the 0.6 wt% Ir@ZrO_2@C.

and 0.56 nm (Fig. 1b). The 0.6 wt% Ir/ZrO_2 presents a typical phase of tetragonal ZrO_2 (Fig. S3), a pore size centered at 0.55 nm (Fig. 1b) and a BET surface area of 108 m^2/g (Table 1).

The STEM images of Ir@UiO-66 and 0.6 wt% Ir@ZrO_2@C are shown in Fig. 2a-b. Apparently, the Ir@UiO-66 has inherited the octahedral morphology from UiO-66. Even after pyrolysis at 873 K in N_2, the obtained Ir@ZrO_2@C maintains the octahedral morphology of UiO-66, only a slightly decrease in the average diameter of crystal size from 160 nm (Ir@UiO-66) to 120 nm (Ir@ZrO_2@C) has been observed. This again proves a partial destruction of the framework of UiO-66 during pyrolysis, which also results in an increase in the roughness of the crystal surface, as reported in the literature [39]. Those are in line with the observed significant drop in micropore surface areas and loss of the micro-porosity after pyrolysis of UiO-66 (Table 1), as also evi-denced by Cao et al [38]. Fig. 2c is the high resolution STEM images of the Ir@ZrO_2@C, which contains isolated ZrO_2 nanoparticles (about 3.0 nm in average), confined by amorphous carbon (high-lighted by the white arrow). No Ir nanoclusters or nanoparticles are evidenced from STEM images, together with high distribution of Ir indicated by EDX-mapping (Fig. 2d), highly dispersed Ir is thus confirmed for the Ir@ZrO_2@C. For the 2.7 wt% Ir/C nanocatalyst, a uniform dispersion of metal, with an average particle size of about 2.0 nm is visualized for Ir/C (Fig. S4). STEM images of the 0.6 wt% Ir/ZrO_2 nanocatalyst are illustrated in Fig. S5, however, it is chal-lenging to determine the particle size of Ir for Ir/ZrO_2. Alternatively, H_2 chemsorption was applied to obtain information about the dis-tribution of iridium on Ir/ZrO_2. As shown in Table S2, the average Ir particle size is calculated to be 1.5 nm.

3.2. Catalytic performance

The LA hydrogenation performance of 0.6 wt% Ir@ZrO_2@C was evaluated under batch conditions in an aqueous solution contain-ing 10 wt% LA at 40 bar H_2 and 453 K. The contrast experiments with 2.7 wt% Ir/C and 0.6 wt% Ir/ZrO_2 nanocatalysts as benchmark catalysts were also performed under the same conditions. Fig. 3a–c shows the individual time-on-line concentration profiles of LA and its products. The Ir/C presents a high activity, with a full LA conver-sion and a GVL yield of 95% in 20 min. This refers to a turnover fre-quency (TOF) of 0.67 s^{-1}, comparable with the value of commercial Ru/C (0.3–0.9 s^{-1}) [38,40]. For Ir/ZrO_2, a medium activity is shown with a TOF value of 0.32 s^{-1}, with a quantitative conversion of LA and a GVL yield of 98% in 80 min. Similar TOF value of Ru/ZrO_2 (0.24 s^{-1}) has been reported in the literature [41]. Ir@ZrO_2@C achieves a LA conversion of 99% and a GVL yield of 98.8% after 10 h reaction, referring to a lower TOF of 0.034 s^{-1}. The significant drop in TOF of the Ir might be originated from the state change of Ir. As previously reported, the TOF value of the single-atom Ru cat-alyst was also much lower (0.17 s^{-1}) than that of the nanoparticle catalyst (0.82 s^{-1}) at 413 K and 10 bar H_2 [38]. Notably, although Ir@ZrO_2@C shows a decreased hydrogenation ability compared to the Ir/C nanocatalyst, it offers an improvement in GVL selectivity (>99%), with almost no generation of other by-products, such as 1,4-pentanediol (PD) and 2-methyltetrahydrofuran (MTHF). Com-paratively, the Ir/C shows an inferior GVL selectivity (85–95%) owing to production of over-hydrogenated PD and MTHF. The defi-ciency of Ir metal in GVL selectivity was also reported by Manzer, with no more than 40% GVL selectivity at nearly full conversion of LA over a 5 wt% Ir/C nanocatalysts at 55 bar H_2 and 423 K after 2 h [14]. This over hydrogenation phenomenon has been encountered by other active metal nanocatalysts during the LA-to-GVL hydro-genation step, such as Rh/C and Ru/TiO_2 [14,41].

The stability of the 2.7 wt% Ir/C nanocatalyst, 0.6 wt% Ir/ZrO_2 nanocatalyst and 0.6 wt% Ir@ZrO_2@C SAC were examined by per-forming multiple recycling tests in a pH = 3 aqueous solution under the applied conditions (Fig. 4). The LA conversion and the GVL yield in different tests were compared before LA reached a full conver-sion level. Observably, the Ir/C nanocatalyst shows a continuous deactivation through recycling runs (Fig. 4a). A drop in LA conver-sion from initial 98% to 59% and a decrease in GVL yield from initial 89% to 52% are observed after three consecutive runs. Similar deac-tivation results of the carbon-supported metal catalysts were also reported in the batch reactor system during recycling tests. For example, Al-Shaal and co-workers demonstrated that a 5 wt% Ru/ C catalyst underwent a 35% decrease in GVL yield through three consecutive runs at 403 K, 12 bar H_2 in a mixed solvent of ethanol and water [22]. Similar results was also reported by Ftouni et al., in

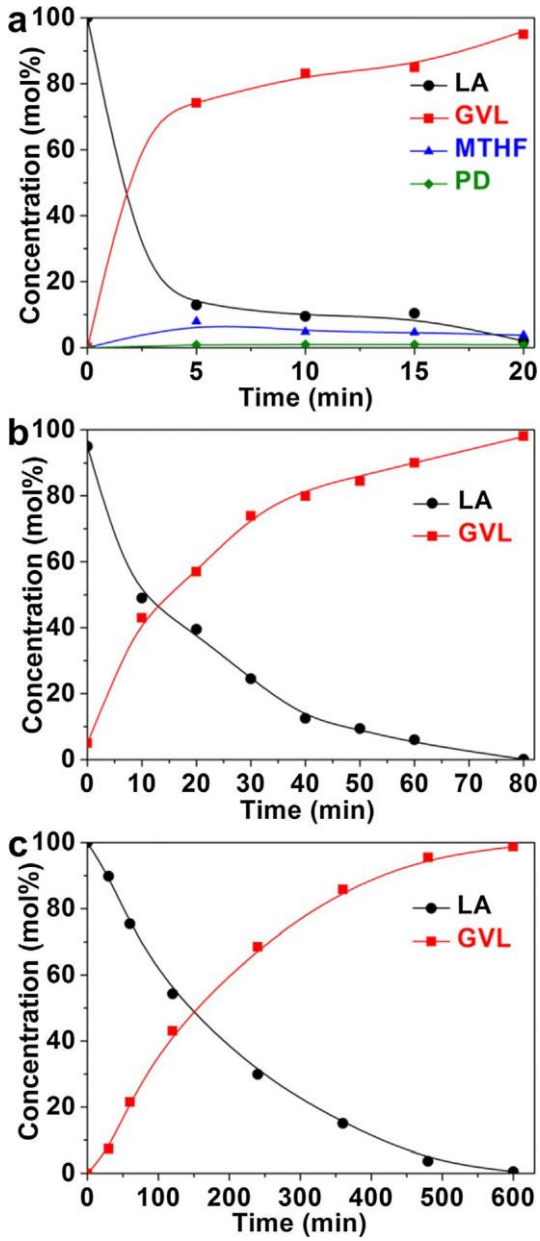

Fig. 3. Time profiles of catalytic conversion of 10 wt% levulinic acid in water using (a) 2.7 wt% Ir/C, (b) 0.6 wt% Ir/ZrO_2 and (c) 0.6 wt% Ir@ZrO_2@C as the catalysts; experimental conditions: T = 453 K, P_{H2} = 40 bar, in an aqueous solution of 10 wt% levulinic acid.

which, a 5 wt% Ru/C catalyst encountered an obvious 30% dropping of GVL yields after five cycles of reuse at 30 bar H_2 and 373 K in dioxane [41]; Recently, Cao et al. also evidenced the apparent deac-tivation of the 5 wt% Ru/C at 10 bar H_2 and 413 K in water, with an almost 30% decrease in LA conversion and a 32% drop in GVL yield through three runs [38]. Since no clear variation of the Ir particle size is observed in STEM images of the spent Ir/C after three times recycling (Fig. S4), sintering as the reason of catalytic activity dete-rioration could be ruled out. N_2 physisorption displays marginal changes in the BET surface area after the recycling runs (Table 1). Notably, about 5.8% leaching of Ir is detected for the 2.7 wt% Ir/C through characterization of the liquid phase after the first recycle by ICP-OES (Table 1), pointing to the leaching of Ir into the reaction solution during the LA hydrogenation. Thus, the leaching of the active metal phase should account for the evidenced deactivation of the Ir/C during the repetitive reuse runs. The 0.6 wt% Ir/ZrO_2 nanocatalyst, also shows a stepwise deactivation during recycling, with a drop in LA conversion from 57% to 45% and also in GVL yield from 56% to 43% after three runs (Fig. 4b). Hutchings et al. have reported the similar deactivation of the Cu/ZrO_2 catalysts, which showed a steady decline in GVL yield from 42% to 34% after four reuse runs at 35 bar H_2 and 473 K [34]. Compared to the Ir/C nanocatalyst, Ir/ZrO_2 shows less loss in activity which possibly benefits from the interaction between Ir and ZrO_2. The BET surface areas of the fresh and spent Ir/ZrO_2 shows limited changes (Table 1). In addition, Ir loading of the spent Ir/ZrO_2 decreased by 6.7% compared to the fresh one, as detected by ICP-OES (Table 1). While the average Ir particle size and dispersion of Ir for Ir/ZrO_2 calculated from H_2 chemsorption changed to 2.0 and 0.49 after recycling (Table S1). As a result, both Ir leaching and sintering are considered as the main cause for the loss of activity of Ir/ ZrO_2. Comparatively, the 0.6 wt% Ir@ZrO_2@C offers an unprece-dented stability for LA hydrogenation, with no drop in LA conver-sion and GVL yield even after seven consecutive runs in a pH = 3 aqueous solution (Fig. 4c). In comparation with the most promising 0.85 wt% Ru/ZrO_2@C [38] recently reported, showing good stability for six consecutive runs at 10 bar H_2 and 413 K, the 0.6 wt% Ir@ZrO_2@C shows a superior stability with no apparent catalyst deactivation at even harsher conditions (a higher temperature of 453 K and 40 bar H_2) upon more runs. In addition, negligible loss of Ir is observed after recycling tests (Table 1). According to the STEM images, the morphology of the spent Ir@ZrO_2@C after seven runs in pH = 3 aqueous solution (Fig. S6a and b), also retains intact and no genesis of Ir nanoparticles are observed (Fig. S6c), suggest-ing the absence of Ir atoms aggregation during recycling. Consis-tently, EDX-mapping analysis (Fig. S6d) further illustrates the uniform distribution of Ir element over the spent Ir@ZrO_2@C. Although N_2 physisorption shows a significant amount of decrease in the surface area from 155 to 59 m^2/g for the spent catalyst (Table 1), which might be attributed to adsorption of reactants/ products or coke deposition in micro-pores, negligible impact on deactivation is shown for the Ir@ZrO_2@C.

Mineral acid, used as the main catalyst for the production of LA from ligno-cellulosic biomass, is inevitably present in the realistic LA product streams, which can bring significant challenges for the catalyst stability [42]. Thus, the development of acid-resistant and robust catalysts with excellent tolerance under severe conditions is highly required for upgrading realistic LA feeds, which can avoid tedious and costly separation and purification processes of remov-ing the acid from LA streams. As a result, the recycling runs for mimicking real LA feed were conducted under pH = 1 conditions with the addition of hydrochloric acid. Considering the present of acid accelerating dehydration step during LA hydrogenation, a higher LA/Ir molar ratio of 1000 was applied with the Ir/C nanocat-alyst for a proper conversion level at a reaction time of 10 min. In Fig. 4d, a gradual catalyst deactivation is already shown for the Ir/C in the second run, with LA conversion decreasing from 70% to 58% and GVL yield from 69% to 55%, respectively. In the third cycles, both of them decrease to no more than 50%, indicating the instabil-ity of Ir/C under more acidic aqueous solution (pH = 1). A similar observation was also reported with Ru/C as the catalyst after injec-tion of mineral acid in a batch system (at 413 K and 10 bar H_2) and a continuous flow system (at 423 K and 35 bar H_2) [25]. Negligible changes in the porosities of the Ir/C are shown during the recycling tests (Table 1). Notably, leaching of Ir into the liquid phase is also detected by ICP-OES, with Ir loss of 3.7 wt% in a pH = 1 aqueous solution (Table 1). This significant Ir leaching phenomenon should account for the main deactivation reason of the Ir/C in the acidic media. For 0.6 wt% Ir/ZrO_2 nanocatalyst, it presents a clear decrease in activity even after one run, with a steady decline in LA conversion from 58% to 23% and also in GVL yield from 53% to

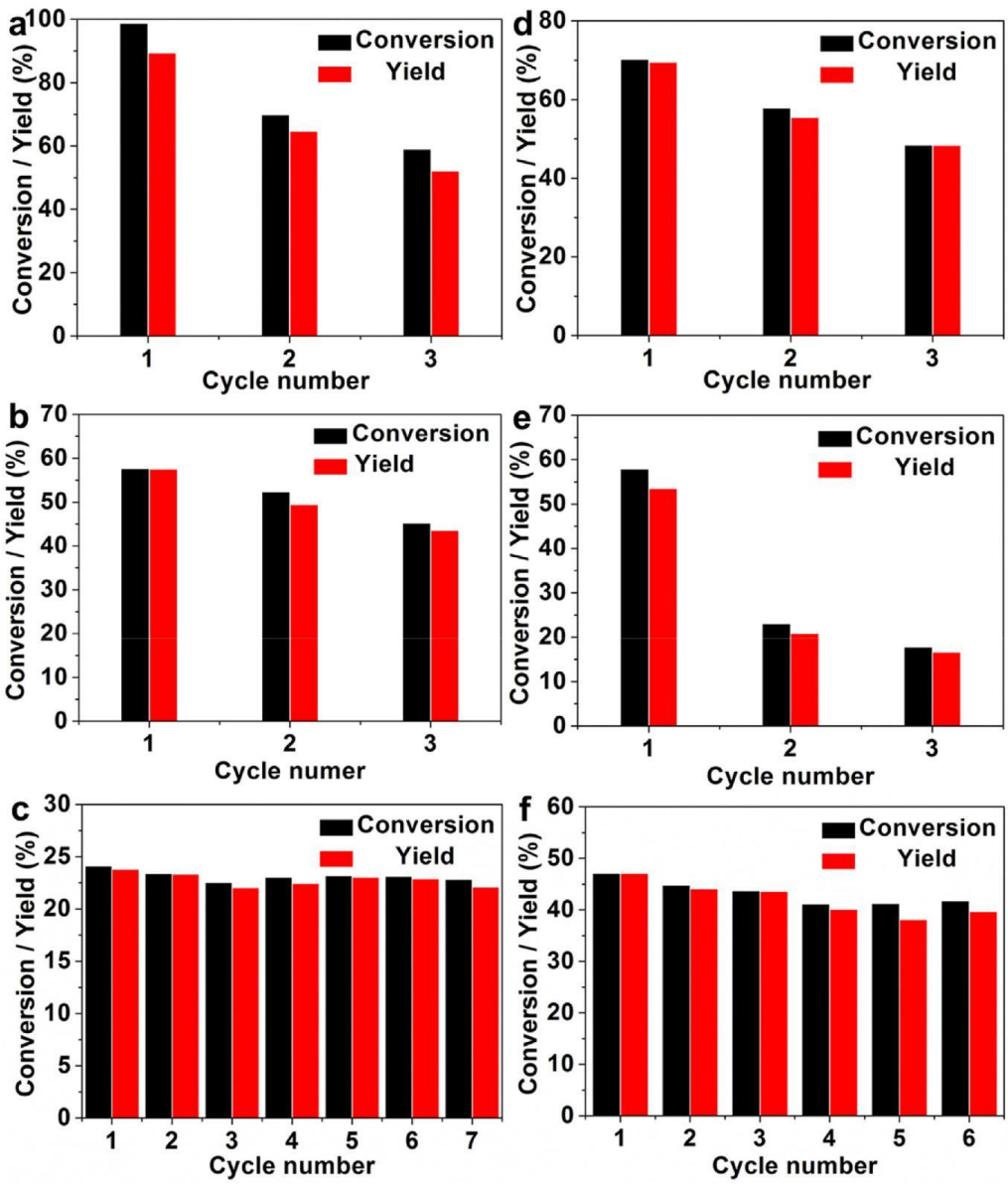

Fig. 4. The recycling experiments of (a) 2.7 wt% Ir/C (10 min), (b) 0.6 wt% Ir/ZrO_2 (20 min) and (c) 0.6 wt% Ir@ZrO_2@C (1 h) in a pH = 3 aqueous solution; the recycling experiments of (d) 2.7 wt% Ir/C (10 min), (e) 0.6 wt% Ir/ZrO_2 (20 min) and (f) 0.6 wt% Ir@ZrO_2@C (1 h) in a pH = 1 aqueous solution; experimental conditions: T = 453 K, P_{H2} = 40 bar, in an aqueous solution of 10 wt% levulinic acid.

20%, and finally dropping to no more than 17% and 16%, separately, in the third run (Fig. 4e). Notably, ICP-OES result illustrates signif-icant loss in Ir loading of Ir/ZrO_2 by 12.5% after recycling, resulting in the catalyst deactivation. In contrast, an ultra-stability of the Ir@ZrO_2@C are shown upon catalyst reuse in a pH = 1 aqueous solution. Only a minor decrease in LA conversion from 47% to 42% and GVL yield from 47% to 40% is observed over the 0.6 wt% Ir@ZrO_2@C after six consecutive runs (Fig. 4f). A significant drop in BET surface areas and a nearly full blockage of micropores are detected for the Ir@ZrO_2@C (Table 1). However, the dramatic loss in porosity seems to have a negligible effect on the performance of catalyst upon recycling, indicating that the intermediate/car-bonaceous species deposition in the Ir@ZrO_2@C does not block the accessibility of the active metal sites. Furthermore, no loss of Ir was detected for the Ir@ZrO_2@C by ICP-OES after LA-to-GVL reac-tions. Recently, an acid-resistant Ru SAC catalyst for LA hydrogena-tion, prepared by a post-modification method, was reported to be re-utilized for three times at 413 K and 10 bar H_2 in a pH = 1 reac-tion media [38]. Comparatively, this Ir@ZrO_2@C, where Ir is loaded by an in-situ synthesis approach, shows enhanced acid tolerance and hydrothermal stability, with no obvious deactivation upon six recycle runs even at harsher conditions (40 bar H_2 and 453 K). The successfully encapsulation of Ir with amorphous carbon by in-situ strategy might prevent the Ir metal sites from sintering and leaching during the LA-to-GVL hydrogenation step.

3.3. Insights into stability and deactivation

Advanced AC-HAADF-STEM measurements with atomic resolu-tion were employed for the visual inspection of Ir location in the 0.6 wt% Ir@ZrO_2@C (Fig. 5). Clearly, no presence of Ir nanoclusters are visualized, while several Ir atoms, representing as bright dots and being denoted in a yellow circle, could be clearly visible in the Ir@ZrO_2@C. An interplanar spacing of 0.29 nm assigned to the (1 1 1) plane of the tetragonal phase ZrO_2 is also detected. Notably, the isolated Ir atoms constantly locate on the Zr column of ZrO_2, in

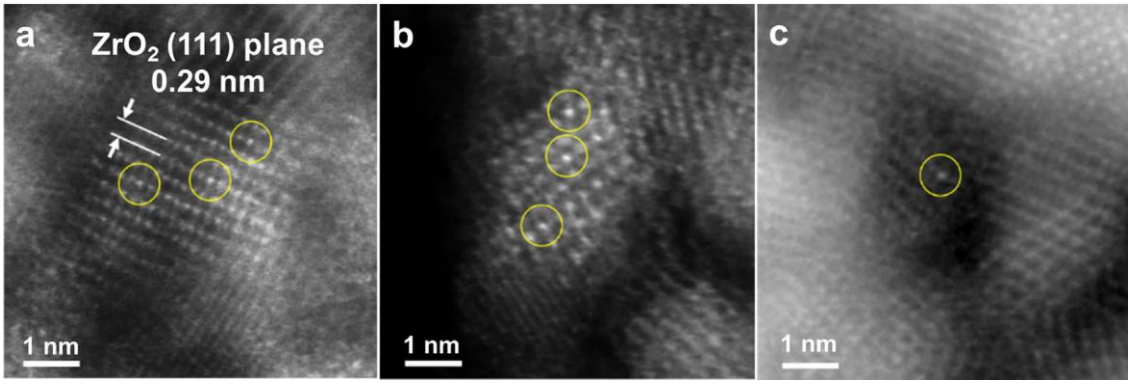

Fig. 5. AC-HAADF-STEM images of the 0.6 wt% Ir@ZrO_2@C SAC.

accordance with the previous observation of the single-atom loca-tion of Ru on ZrO_2 support [41]. The single-atom Ir sites in the Ir@ZrO_2@C are achieved by utilizing the defect engineering of UiO-66 structure. Highly isolated Zr-cluster nodes are connected and separated by organic linkers, forming molecular-level cages in the UiO-66 structure [43]. However, the addition of glacial acetic acid as modulator is reported to produce defect during the forma-tion of UiO-66 via terminating some of the Zr-cluster nodes with missing framework linkage [36,37]. The tantalizing AOH sites gen-erated by the defects of the missing linkers on the Zr-cluster nodes during assembly of UiO-66, probably serve as the anchor sites for Ir precursor [44–47], and the small cages can spatially confine iso-lated metal atoms to prevent further metal migration [48]. During the following high-temperature pyrolysis, the organic linkers are transformed into amorphous carbon, covering and isolating on the outside of tetragonal phase ZrO_2. Therefore, the employment of UiO-66 structure during the in-situ synthesis method is pivotal for achieving the high, improved Ir dispersion in our case.

To understand the significant discrepancy in catalyst perfor-mance between the contrast catalysts (2.7 wt% Ir/C nanocatalyst and 0.6 wt% Ir/ZrO_2 nanocatalyst) and 0.6 wt% Ir@ZrO_2@C SAC, XPS was also conducted to examine the surface properties of differ-ent catalysts before and after the multiple reuse in the pH = 3 aqueous solution. For the Ir/C nanocatalyst, the C 1s signal (Fig. 6a) can be deconvoluted into three peaks at 287.8, 285.6 and 284.4 eV, assigned to C@O groups from the carboxyl group or esters, CAO groups from etheric and phenolic alcoholic species and CAC groups from aromatic species, respectively [49]. The O 1s signal (Fig. 6b) is consist of three major constituents centered at 533.0, 531.5 and 530.0 eV, separately corresponding to CAO, C@O and IrAO species [50]. An increase in surface C@O species is visualized in both of C 1s and O 1s with the spent Ir/C after three recycling runs, which could be originated from the deposited spe-cies (LA, GVL and containing C@O coke) during catalysis. The Ir 4f spectral region (Fig. 6c) reveals three major contributions on the surface of the Ir/C, which could be assigned to Ir^{4+} (62.4 and 65.4 eV), Ir^{d+} (61.5 and 64.5 eV) and metallic Ir (60.9 and 63.9 eV) species [51–53]. The additional peaks at 63.3 and 66.3 eV are satel-lite peaks of Ir^{4+} species, as also reported in other deconvolutions [54,55]. The presence of these cation Ir surface species is probably derived from the oxidation of air during storage and transporta-tion, along with the coordination between Ir and the oxygen-rich species on the surface of carbon, as confirmed by the CAO species in C 1s and IrAO and C@O species in O 1s [56]. Significant differ-ence in the Ir 4f region of the fresh and three-times recycled Ir/C catalyst is observed. The fresh Ir/C sample mostly shows metallic Ir species (70% of total Ir $3d_{5/2}$ area), as well as some amount of Ir^{d+} (20% of total Ir $3d_{5/2}$ area) and Ir^{4+} (10% of total Ir $3d_{5/2}$ area) from IrO_x and IrO_2 species, separately. In comparison, the three-times recycled Ir/C catalyst displays a sharp drop in metallic Ir (33% of total Ir $3d_{5/2}$ area) and a slightly increase in Ir^{d+} species (41% of total Ir $3d_{5/2}$ area) in Fig. 6c, probably caused by combina-tion of surface metallic Ir leaching into the solution and partial Ir^{4+} reduction to Ir^{d+} during reaction hydrogenation conditions. The Ir leaching is indeed observed by ICP-OES analysis (Table 1). Again, a slight decrease in the IrAO group is observed with the spent Ir/ C compared to the fresh Ir/C in O 1s XPS (Fig. 6b), confirming the reduction of Ir^{4+}. In terms of the Ir/ZrO_2 nanocatalyst, O 1s XPS spectra mainly show the emergency of CAO group and increase in C@O due to the adsorption of LA, GVL and coke species on the surface after three consecutive runs under pH = 3 (Fig. 7a). Negligi-ble change in Zr-O groups is observed, as also confirmed by the nearly unchanged Zr 3d spectra after recycling (Fig. 7b). In the spectra of Ir 4f (Fig. 7c), the fresh Ir/ZrO_2 mainly contains Ir^{4+}, Ir^{d+}, and metallic Ir species. After recycling, an obvious increase in metallic Ir and concomitant disappearance in Ir^{4+} and Ir^{d+} spe-cies are observed. These changes are possibly caused by the partial Ir^{4+} and Ir^{d+} reduction to metallic Ir during reaction hydrogenation conditions. The reduction of the metal species can lead to the growth of metal particle size, as evidenced by the increased Ir par-ticle size (2.0 nm) of Ir/ZrO_2 calculated from H_2 chemsorption (Table S1). In addition, the reduction of the metal species can be related to the decrease in interaction between metal and support, resulting in the subsequent leaching of Ir species into the solution, as indicated by ICP-OES (Table 1).

Notably, marginal changes are observed between the fresh and spent Ir@ZrO_2@C SAC compared to those with the Ir/C and Ir/ZrO_2 nanocatalysts in XPS spectra (Fig. 8). A minor increase in C@O spe-cies is observed for the spent catalyst after the recycling tests in C 1s (Fig. 8a) and more apparent in O 1s (Fig. 8b) XPS spectra. This raise in surface C@O species should be attributed to the adsorbed species containing C@O groups (LA, GVL and coke species) on the surface, as also evidenced by the significant drop in micro-porosity of the recycled Ir@ZrO_2@C (Table 1). The Zr 3d XPS spectra reveals no obvious change (Fig. 8c), in line with marginal changes of ZrAO groups in O 1s (Fig. 8b). The Ir 4f XPS spectra (Fig. 8d) shows that the Ir species mainly exist as the Ir^{d+} on the Ir@ZrO_2@C surface, and no apparent intensity change or new features is observed with the seven-times recycled Ir@ZrO_2@C catalyst. The only existence of Ir^{d+} species indicates uniform distribution of iso-lated Ir atoms and a possible interaction between Ir and nano-tetraganol ZrO_2. Such interaction, which affects the valence state of metal and improves the stability of single atoms, has already been reported with SACs [26,57]. In addition, a much weaker inten-sity of features (1/200) in Ir 4f region is observed for the fresh Ir@ZrO_2@C than that of the fresh Ir/C, although at a 4.5 times lower

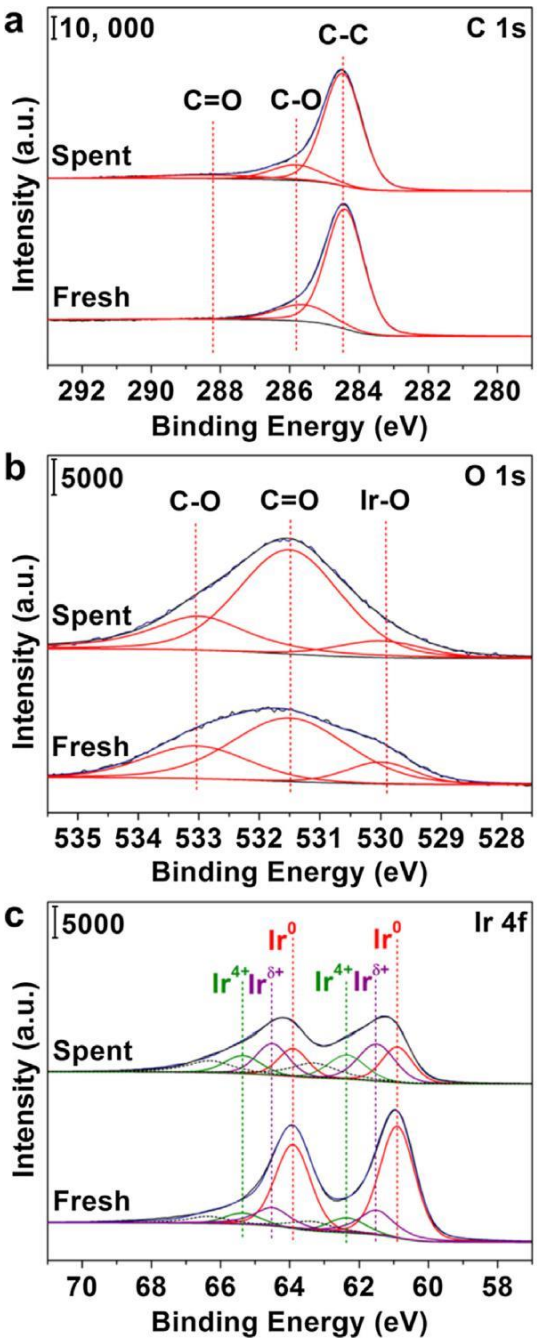

Fig. 6. (a) C 1s, (b) O 1s, and (c) Ir 4f XPS of the fresh and spent (three-times recycled) 2.7 wt% Ir/C nanocatalyst in a pH = 3 aqueous solution.

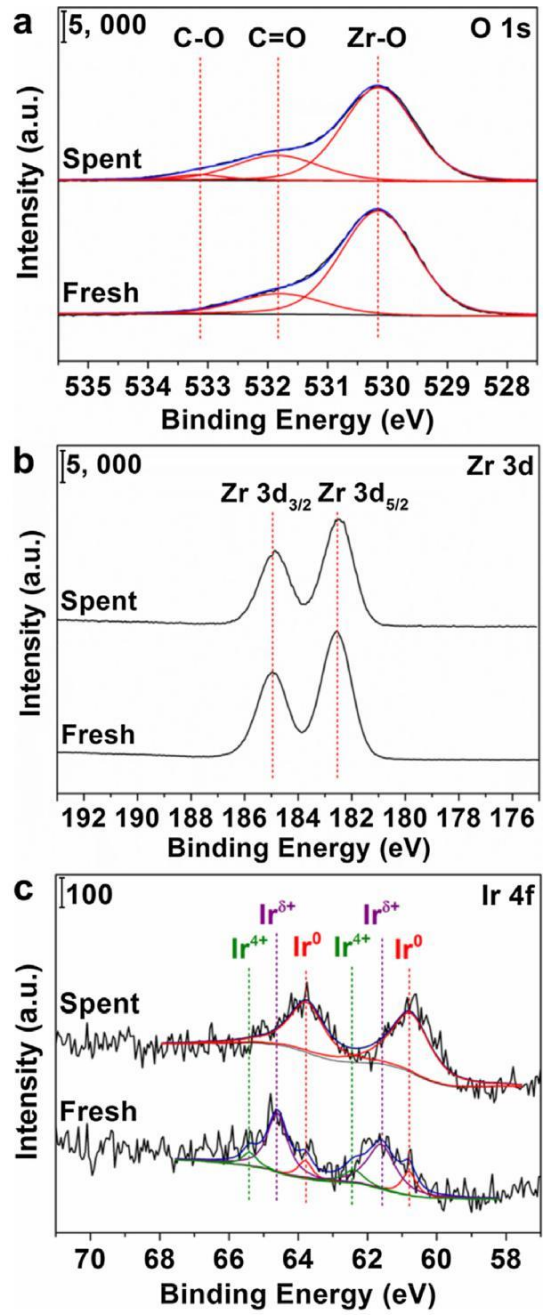

Fig. 7. (a) O 1s, (b) Zr 3d, and (c) Ir 4f XPS of the fresh and spent (three-times recycled) 0.6 wt% Ir/ZrO_2 nanocatalyst in a pH = 3 aqueous solution.

content of Ir. This again points to quite amount of Ir atoms, are located inside of the Ir@ZrO_2@C, which are not detectable by XPS owing to the coverage by amorphous carbon. At this applied reac-tion temperature (453 K), the hydrogenation metal exhibits a more dominant impact for LA hydrogenation than support acidity. From the activity data (Fig. 3a–c), both the Ir/C (TOF = 0.67 s^{1}) and Ir/ ZrO_2 nanocatalyst (TOF = 0.32 s^{1}) shows a much higher TOF value than Ir@ZrO_2@C (TOF = 0.034 s^{1}), pointing to a higher hydrogena-tion ability of Ir nanoparticle compared to Ir single atoms. The sig-nificant change in activity should be directly correlated to the valence state change of Ir. The domain metallic Ir state of nanopar-ticle catalyst shows a higher activity in LA hydrogenation than the only Ir^{d+} species of SAC [58]. In addition, the clear deactivation observed for the recycled Ir/C, is mainly attributed to the loss of metallic Ir species in XPS, consistently indicating that the metallic Ir is more active for LA hydrogenation than the Ir^{d+} species. Although the Ir^{d+} species in SAC shows a dropping in hydrogena-tion ability, deep hydrogenation reactions forming byproducts can be efficiently depressed and high GVL selectivity is thus achieved. Similarly, the utilization of Pt single-atom catalysts, have been reported for achieving the excellent selectivity in hydrogena-tion of 1,3-butadiene with the presence of propene, wherein form-ing isolated Pt cation sites can efficiently avoid propene hydrogenation by tuning down the hydrogenation ability [27,58].

To further characterize the electronic properties and structure information of the Ir sites in the Ir@ZrO_2@C SAC, FT-IR spectra of CO measurements were conducted with Ir@ZrO_2, which was

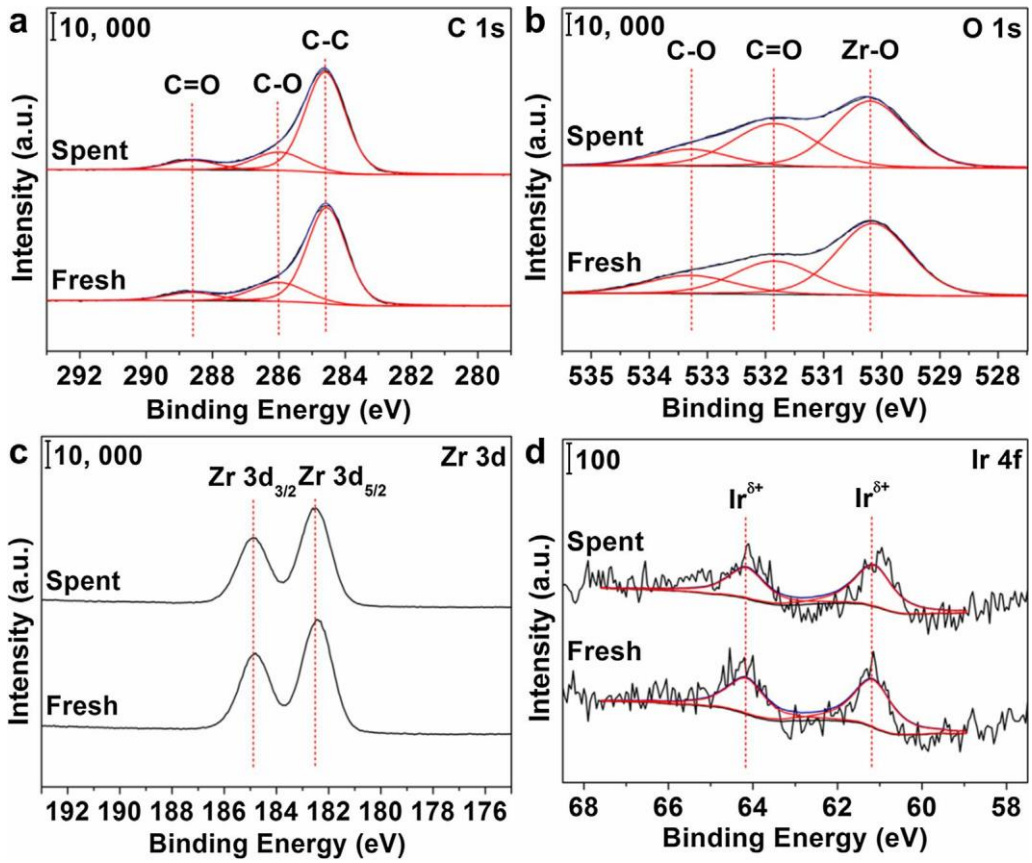

Fig. 8. (a) C 1s, (b) O 1s, (c) Zr 3d, and (d) Ir 4f XPS of the fresh and spent (seven-times recycled) 0.6 wt% Ir@ZrO_2@C SAC in a pH = 3 aqueous solution.

obtained by removing the amorphous carbon by thermal treatment at 873 K for 5 h under air atmosphere. A good spectral quality with improved resolution is obtained without the interference of carbon materials at a temperature of 85 K (Fig. 9a), and spectral features are thus visualized for the material even with the low loading of Ir. The spectra can be divided into a high (2180–1950 cm ^{1}) and low frequency region (1950–1750 cm ^{1}), corresponding to car-bonyl species adsorbed in a linear and bridged fashion. The spectra show no CO adsorption in the low-frequency region, indicating no bridged carbonyl species at variable pressure and thus the absence of dimer or metal clusters [57], consistent with the AC-HAADF-STEM results that Ir species are present as isolated Ir single-atom sites on Ir@ZrO_2@C. Four spectral features at 2180, 2152, 2120 and 2080 cm ^{1} could be visualized with the stepwise introduction of CO from 0 to 10 mbar. The feature at 2152 cm ^{1} appears only above 1.50 mbar CO, assigned to physically adsorbed CO species. The feature first at 2180 cm ^{1} at low CO pressure and then red-shifted to 2168 cm ^{1} is assigned to COAZr^{4+} species, and another feature at 2120 cm ^{1} is correlated to COAZr^{3+} sites [59,60]. Nota-bly, the feature at 2080 cm ^{1}, appeared at a low CO coverage, can be ascribed to CO linearly adsorbed on Ir sites [61,62]. Com-pared to CO adsorbed on metallic Ir^{0} sites at 2050 cm ^{1} with Ir/ CeO_2 [63], Ir/SiO_2 [64], the blue-shifted signal indicates that the adsorbed Ir sites are in cationic form. Considering the only exis-tence of slightly positively charged Ir^{d+} species by XPS (Fig. 8d), this signal should be ascribed to Ir^{d+}ACO species. Comparatively, the about 30 cm ^{1} blue-shift of this signal indicates a strong modifica-tion of Ir electronic structure by supporting on nano-tetragonal ZrO_2, which might benefit the stabilization of Ir single atoms on the support as well as the origin of ultra-stability for LA-to-GVL hydrogenation. In addition, no shift of the signal at 2080 cm ^{1} is visualized with the increase of CO pressure, which again confirms the atomic dispersion of Ir^{d+} species on ZrO_2.

For obtaining further insights of the interaction between Ir and nano-tetragonal ZrO_2 support, H_2-TPR analysis has been also per-formed for the Ir/C nanocatalyst, Ir/ZrO_2 nanocatalyst and Ir@ZrO_2@C SAC (Fig. 9b). For the Ir/C, the signals in the region above 500 K are strongly interfered by the various and complicate carbon species from the support. Only a small signal centered at 355 K is distinguished and assigned to the reduction of oxidized Ir [52]. This correlates well with XPS data (Fig. 6c), which shows the existence of minor Ir oxide species and major metallic Ir spe-cies. Similar reduction signal at about 360 K has also been observed on Ir nanocatalysts [52,65]. 0.6 wt% Ir/ZrO_2 nanocatalyst shows two reduction peaks below 500 K. One signal at 370 K should be ascribed to the signal of Ir oxides, and the other signal at a higher temperature of 435 K is assigned to the Ir^{d+} species interacted with t-ZrO_2 support, in coincidence with the existence of Ir^{4+}and Ir^{d+} species in XPS results (Fig. 7c). Similar reduction signal of Ir/ CeO_2-ZrO_2 was also reported in the literature [66]. Compared to the Ir/ZrO_2 nanocatalyst, the Ir@ZrO_2@C SAC shows an apparent reduction signal at higher temperature of 455 K, indicating a stron-ger interaction between Ir^{d+} and ZrO_2. Combining the IR-CO and XPS results, this enhanced interaction mainly origins from the modification of the electronic properties of Ir upon supporting on nano-tetragonal ZrO_2. Such modification can not only significantly improve the metal-support interactions by preventing leaching and aggregation of expensive Ir metal even under harsh conditions, but also enhance the GVL selectivity by tuning down the hydro-genation ability. In addition, the spatial confinement of amorphous carbon further prevents the growing and migration of nano-tetragonal ZrO_2 and Ir metal sites, maintaining the structural integ-

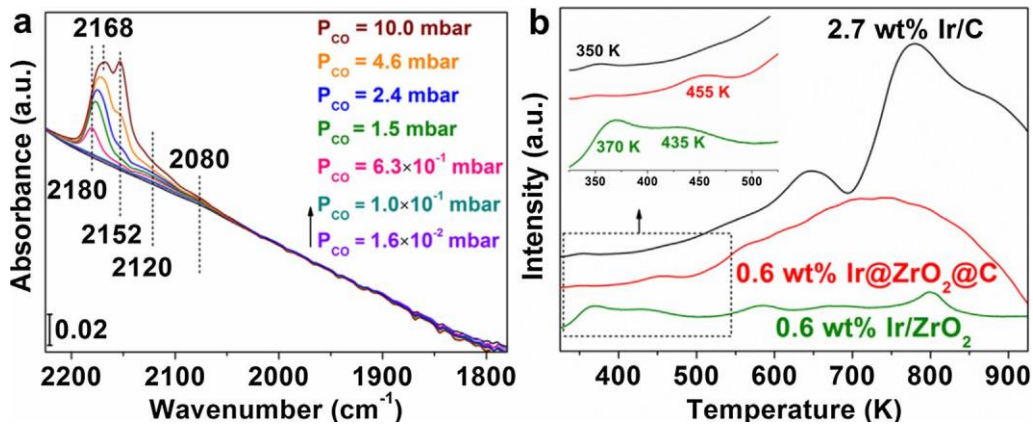

Fig. 9. (a) FT-IR spectra of CO adsorbed on Ir@ZrO_2 at 85 K, and CO was introduced into the cell stepwise from 0 to 10.0 mbar; (b) H_2-TPR analysis of the 2.7 wt% Ir/C nanocatalyst, 0.6 wt% Ir/ZrO_2 nanocatalyst and 0.6 wt% Ir@ZrO_2@C SAC.

rity during the further treatments and catalysis. Furthermore, pre-vious studies reported single-atom Ir with a quite low Ir loading of around 0.01 wt% on different oxide supports, such as FeO_x [67] and MgO [68]. In our case, a fully atomically dispersed Ir SAC with a higher metal loading up to 0.6 wt% is achieved via an in-situ syn-thesis method. Encouragingly, the novel developed SAC has shown an outstanding durability for the selective hydrogenation of LA to GVL in liquid phase under highly acidic and harsh conditions. This work provides not only an efficient approach for the preparation of acid-resistant SACs via utilizing the skeletons of metal-organic framework, but also shows a good example on tuning the metal-support interactions for achieving ultra-stability and enhanced selectivity in catalysis.

4. Conclusions

In conclusion, an ultra-stable 0.6 wt% Ir@ZrO_2@C SAC has been successfully developed by a novel in-situ synthesis approach via employing metal-organic framework as scaffold. Catalytic perfor-mance, especially stability of this Ir@ZrO_2@C SAC has been evalu-ated and compared to the benchmark 2.7 wt% Ir/C and 0.6 wt% Ir/ ZrO_2 nanocatalyst in selective hydrogenation of LA to GVL at 453 K and 40 bar H_2 in a high protic pH = 3 or pH = 1 aqueous solu-tion. Both Ir/C and Ir/ZrO_2 are active, but not stable, observed with apparent deactivation upon consecutive reuse tests in both pH = 3 and pH = 1 aqueous solutions. Through the characterizations of the catalyst state before and after reactions, the deactivation of the Ir/C and Ir/ZrO_2 is primarily attributed to the loss of active sites by metal leaching/sintering during reactions. In contrast, the Ir@ZrO_2@C SAC displays an inferior activity, but excellent GVL selectivity and ultra-stability. Notably, marginal decrease in cat-alytic performance has been observed with this SAC in seven repet-itive cycles (pH = 3) and six repetitive cycles (pH = 1) under hydrothermal, protic and polar liquid phase conditions. Extensive characterizations, such as AC-HAADF-STEM, XPS, IR-CO as well as H_2-TPR characterizations display a well-defined structure of the Ir@ZrO_2@C, with fully atomic dispersion of Ir^{d+} on nano-tetragonal ZrO_2 (3.0 nm), confined and isolated by the amorphous carbon. No structural changes and formation of Ir nanoparticles/ nanoclusters by metal aggregation are observed during the recy-cling runs. The ultra-stability of the Ir@ZrO_2@C under acidic condi-tions mainly arises from the enhanced interactions between the isolated Ir^{d+} species and nano-tetragonal ZrO_2 support, as well as the confinement of the amorphous carbon. Overall, the novel in-situ synthesis method and successful synthesis of an ultra-stable Ir@ZrO_2@C SAC will be of great help for developing ultra-stable and acid-resistant catalysts for hydrogen-assisted biomass val-orizations and other energy-related conversions.

Acknowledgements

The National Key Projects for Fundamental Research and Devel-opment of China (2018YFB1501600 and 2016YFA0202801), National Natural Science Foundation of China (21703238, 21673228, 21690084 and 21690080), and the Strategic Priority Research Program of the Chinese Academy of Sciences (XDB17020100 and XDA 21060200) are acknowledged for financial support. Dr Rui Chen, Dr Xiaoli Pan, Jian Li and Prof. Tiehong Chen are acknowledged for the XPS, STEM, TPR measurements and the fruitful discussion in XPS, respectively. The authors thank Diamond Light Source for access and support in the use of the electron Phys-ical Science Imaging Centre (Proposal EM18909), and the staff (Dr Christopher Allen and Dr Chen Huang) of beamlines E01 for assistance.

References

[1] H. Zhao, J.E. Holladay, H. Brown, Z.C. Zhang, Science 316 (2007) 1597–1600.
[2] C.-H. Zhou, X. Xia, C.-X. Lin, D.-S. Tong, J. Beltramini, Chem. Soc. Rev. 40 (2011) 5588–5617.
[3] D.M. Alonso, S.G. Wettstein, J.A. Dumesic, Chem. Soc. Rev. 41 (2012) 8075– 8098.
[4] D.M. Alonso, J.Q. Bond, J.A. Dumesic, Green Chem. 12 (2010) 1493–1513.
[5] J.J. Bozell, G.R. Petersen, Green Chem. 12 (2010) 539–554.
[6] J.C. Serrano-Ruiz, J.A. Dumesic, Energ. Environ. Sci. 4 (2011) 83–99.
[7] D.W. Rackemann, W.O. Doherty, Biofuel. Bioprod. Bio. 5 (2011) 198–214.
[8] V. Pace, P. Hoyos, L. Castoldi, P. Domínguez de María, A.R. Alcántara, ChemSusChem 5 (2012) 1369–1379.
[9] F.D. Pileidis, M.-M. Titirici, ChemSusChem 9 (2016) 562–582.
[10] D.M. Alonso, S.G. Wettstein, J.A. Dumesic, Green Chem. 15 (2013) 584–595.
[11] M. Amanda-Lynn, P.J. Alaimo, Chem.–Eur. J. 16 (2010) 4970–4980.
[12] W. Deng, Q. Zhang, Y. Wang, J. Energy Chem. 24 (2015) 595–607.
[13] S. Van de Vyver, J. Geboers, W. Schutyser, M. Dusselier, P. Eloy, E. Dornez, J.W. Seo, C.M. Courtin, E.M. Gaigneaux, P.A. Jacobs, B.F. Sels, ChemSusChem 5 (2012) 1549–1558.
[14] L.E. Manzer, Appl. Cata. A–Gen. 272 (2004) 249–256.
[15] Z.-P. Yan, L. Lin, S. Liu, Energ. Fuel. 23 (2009) 3853–3858.
[16] C. Ortiz-Cervantes, M. Flores-Alamo, J.J. García, ACS Catal. 5 (2015) 1424–1431.
[17] J.-P. Lange, R. Price, P.M. Ayoub, J. Louis, L. Petrus, L. Clarke, H. Gosselink, Angew. Chem. Int. Ed. 49 (2010) 4479–4483.
[18] W. Li, J.-H. Xie, H. Lin, Q.-L. Zhou, Green Chem. 14 (2012) 2388–2390.
[19] S. Wang, V. Dorcet, T. Roisnel, C. Bruneau, C. Fischmeister, Organometallics 36 (2017) 708–713.

[20] K. Yan, Y. Yang, J. Chai, Y. Lu, Appl. Catal. B–Environ. 179 (2015) 292–304.
[21] B. Cai, X.-C. Zhou, Y.-C. Miao, J.-Y. Luo, H. Pan, Y.-B. Huang, A.C.S. Sustain, Chem. Eng. 5 (2017) 1322–1331.
[22] M.G. Al-Shaal, W.R.H. Wright, R. Palkovits, Green Chem. 14 (2012) 1260–1263.
[23] S.G. Wettstein, J.Q. Bond, D.M. Alonso, H.N. Pham, A.K. Datye, J.A. Dumesic, Appl. Catal. B–Environ. 117–118 (2012) 321–329.
[24] O.A. Abdelrahman, A. Heyden, J.Q. Bond, ACS Catal. 4 (2014) 1171–1181.
[25] D.J. Braden, C.A. Henao, J. Heltzel, C.C. Maravelias, J.A. Dumesic, Green Chem. 13 (2011) 1755–1765.
[26] A. Wang, J. Li, T. Zhang, Nat. Rev. Chem. 2 (2018) 65–81.
[27] F.R. Lucci, J. Liu, M.D. Marcinkowski1, M. Yang, L.F. Allard, M. Flytzani-Stephanopoulos, C.H. Sykes, Nat. Commun. 6 (2015) 8850–8857.
[28] W. Liu, Y. Chen, H. Qi, L. Zhang, W. Yan, X. Liu, X. Yang, S. Miao, W. Wang, C. Liu, A. Wang, J. Li, T. Zhang, Angew. Chem. Int. Ed. 57 (2018) 7071–7075.
[29] G. Liu, A.W. Robertson, M.M.-J. Li, W.C.H. Kuo, M.T. Darby, M.H. Muhieddine, Y.-C. Lin, K. Suenaga, M. Stamatakis, J.H. Warner, S.C.E. Tsang, Nat. Chem. 9 (2017) 810–816.
[30] R. Malacea, R. Poli, E. Manoury, Coordin. Chem. Rev. 254 (2010) 729–752.
[31] X. Du, Y. Liu, J. Wang, Y. Cao, K. Fan, Chinese J. Catal. 34 (2013) 993–1001.
[32] N.S. Date, A.M. Hengne, K.W. Huang, R.C. Chikate, C.V. Rode, Green Chem. 20 (2018) 2027–2037.
[33] W. Li, H. Huang, H. Li, W. Zhang, H. Liu, Langmuir 24 (2008) 8358–8366.
[34] S. Ishikawa, D.R. Jones, S. Iqbal, C. Reece, D.J. Morgan, D.J. Willock, P.J. Miedziak, J.K. Bartley, J.K. Edwards, T. Murayama, W. Ueda, G.J. Hutchings, Green Chem. 19 (2017) 225–236.
[35] W. Luo, U. Deka, A.M. Beale, E.R.H. van Eck, P.C.A. Bruijnincx, B.M. Weckhuysen, J. Catal. 301 (2013) 175–186.
[36] S. Andreas, R. Pascal, G. Adelheid, L. Jann, W. Florian, W. Michael, B. Peter, Chem.–Eur. J. 17 (2011) 6643–6651.
[37] H. Wu, Y.S. Chua, V. Krungleviciute, M. Tyagi, P. Chen, T. Yildirim, W. Zhou, J. Am. Chem. Soc. 135 (2013) 10525–10532.
[38] W. Cao, W. Luo, H. Ge, Y. Su, A. Wang, T. Zhang, Green Chem. 19 (2017) 2201–2211.
[39] M.Y. Masoomi, A. Morsali, Coord. Chem. Rev. 256 (2012) 2921–2943.
[40] W. Luo, M. Sankar, A.M. Beale, Q. He, C.J. Kiely, P.C.A. Bruijnincx, B.M. Weckhuysen, Nat. Commun. 6 (2015) 6540–6549.
[41] J. Ftouni, A. Muñoz-Murillo, A. Goryachev, J.P. Hofmann, E.J.M. Hensen, L. Lu, C. J. Kiely, P.C.A. Bruijnincx, B.M. Weckhuysen, ACS Catal. 6 (2016) 5462–5472.
[42] B. Girisuta, L.P.B.M. Janssen, H.J. Heeres, Ind. Eng. Chem. Res. 46 (2007) 1696–1708.
[43] J.H. Cavka, S. Jakobsen, U. Olsbye, N. Guillou, C. Lamberti, S. Bordiga, K.P. Lillerud, J. Am. Chem. Soc. 130 (2008) 13850–13851.
[44] M. Rimoldi, A.J. Howarth, M.R. DeStefano, L. Lin, S. Goswami, P. Li, J.T. Hupp, O. K. Farha, ACS Catal. 7 (2017) 997–1014.
[45] R.J. Marshall, R.S. Forgan, Eur. J. Inorg. Chem. 2016 (2016) 4310–4331.
[46] H.G.T. Nguyen, N.M. Schweitzer, C.-Y. Chang, T.L. Drake, M.C. So, P.C. Stair, O.K. Farha, J.T. Hupp, S.T. Nguyen, ACS Catal. 4 (2014) 2496–2500.
[47] D. Yang, S.O. Odoh, T.C. Wang, O.K. Farha, J.T. Hupp, C.J. Cramer, L. Gagliardi, B. C. Gates, J. Am. Chem. Soc. 137 (2015) 7391–7396.
[48] Y. Chen, S. Ji, C. Chen, Q. Peng, D. Wang, Y. Li, Joule 2 (2018) 1242–1264.
[49] C. Hontoria-Lucas, A.J. López-Peinado, J.d.D. López-González, M.L. Rojas-Cervantes, R.M. Martín-Aranda, Carbon 33 (1995) 1585–1592.
[50] G. de la Puente, J.J. Pis, J.A. Menéndez, P. Grange, J. Anal. Appl. Pyrol. 43 (1997) 125–138.
[51] V. Pfeifer, T.E. Jones, J.J. Velasco Vélez, C. Massué, M.T. Greiner, R. Arrigo, D. Teschner, F. Girgsdies, M. Scherzer, J. Allan, M. Hashagen, G. Weinberg, S. Piccinin, M. Hävecker, A. Knop-Gericke, R. Schlögl, Phys. Chem. Chem. Phys. 18 (2016) 2292–2296.
[52] G.K. Wertheim, H.J. Guggenheim, Phys. Rev. B 22 (1980) 4680–4683.
[53] S.J. Freakley, J. Ruiz-Esquius, D.J. Morgan, Surf. Interface Anal. 49 (2017) 794–799.
[54] J. Breen, R. Burch, J. Gomez-Lopez, K. Griffin, M. Hayes, Appl. Cata. A–Gen. 268 (2004) 267–274.
[55] L.I. Kuznetsova, N.I. Kuznetsova, S.V. Koscheev, V.I. Zaikovskii, A.S. Lisitsyn, K. M. Kaprielova, N.V. Kirillova, Z. Twardowski, Appl. Cata. A-Gen. 427 (2012) 8–15.
[56] D.W. Rackemann, W.O. Doherty, Biofuel. Bioprod. Bio. 5 (2011) 198–214.
[57] B. Qiao, A. Wang, X. Yang, L.F. Allard, Z. Jiang, Y. Cui, J. Liu, J. Li, T. Zhang, Nat. Chem. 3 (2011) 634–641.
[58] Z. Zhang, Y. Zhu, H. Asakura, B. Zhang, J. Zhang, M. Zhou, Y. Han, T. Tanaka, A. Wang, T. Zhang, N. Yan, Nat. Commun. 8 (2017) 16100–16109.
[59] C. Morterra, G. Cerrato, S. Di Ciero, Appl. Surf. Sci. 126 (1998) 107–128.
[60] T.M. Miller, V.H. Grassian, Catal. Lett. 46 (1997) 213–221.
[61] M. Mihaylov, E. Ivanova, F. Thibault-Starzyk, M. Daturi, L. Dimitrov, K. Hadjiivanov, J. Phys. Chem. B 110 (2006) 10383–10389.
[62] J. Lin, L. Li, X. Pan, X. Wang, Y. Cong, T. Zhang, S. Zhu, AIChE J. 62 (2016) 3973–3981.
[63] T.-S. Nguyen, G. Postole, S. Loridant, F. Bosselet, L. Burel, M. Aouine, L. Massin, P. Gélin, F. Morfin, L. Piccolo, J. Mater. Chem. A 2 (2014) 19822–19832.
[64] H. Rojas, G. Díaz, J.J. Martínez, C. Castañeda, A. Gómez-Cortés, J. Arenas-Alatorre, J. Mol. Catal. A-Chem. 363–364 (2012) 122–128.
[65] J. Lu, P. Serna, C. Aydin, N.D. Browning, B.C. Gates, J. Am. Chem. Soc. 133 (2011) 16186–16195.
[66] V.O. Dundich, V.A. Yakovlev, Chem. Sustain. Dev. 17 (2009) 527–532.
[67] J. Lin, A. Wang, B. Qiao, X. Liu, X. Yang, X. Wang, J. Liang, J. Li, J. Liu, T. Zhang, J. Am. Chem. Soc. 135 (2013) 15314–15317.
[68] A.S. Hoffman, L.M. Debefve, S. Zhang, J.E. Perez-Aguilar, E.T. Conley, K.R. Justl, I. Arslan, D.A. Dixon, B.C. Gates, ACS Catal. 8 (2018) 3489–3498.